




Fabrication ternary dual Z-scheme InVO₄/Bi₂S₃/g-C₃N₄ heterojunction photocatalyst for the highly efficient visible-light-driven degradation of Reactive Blue 19

Yuzhen Li^{1,*} , Siyang Tan¹, Yachu Meng¹, Yunsheng Xia², Lizhen Gao^{1,3}, and Wenjun Chen^{4,*}

¹College of Environmental Science and Engineering, Taiyuan University of Technology, 79 Yingze Street, Wanbailin District, Taiyuan 030024, China

²Department of Chemistry, Bohai University, Jinzhou 121013, China

³School of Mechanical Engineering, University of Western Australia, 35 Stirling Highway, Perth, WA 6009, Australia

⁴Shanxi Provincial People's Hospital, Taiyuan 030012, China

Received: 22 October 2021

Accepted: 24 April 2022

Published online:

20 May 2022

© The Author(s), under exclusive licence to Springer Science+Business Media, LLC, part of Springer Nature 2022

ABSTRACT

A novel visible-light-driven InVO₄/Bi₂S₃/g-C₃N₄ (VBSCN) nanocomposite photocatalyst was successfully synthesized by a wet-impregnation method. The phase, morphology, chemical composition, microstructure, and optical properties of the prepared pure g-C₃N₄ and ternary InVO₄/Bi₂S₃/g-C₃N₄ heterojunctions were measured in detail by various characterization techniques, including powder XRD, FT-IR, TEM, SEM, BET, UV-Vis DRS, PL, the photocurrent response, and EIS analyses. The fabricated nanocomposites Bi₂S₃/g-C₃N₄ with the InVO₄ doping mass ratio of 5% exhibited superior photocatalytic degradation of Reactive blue 19 dye under visible light irradiation. Furthermore, O₂⁻ was identified as the main active species by free radical trapping. This efficient catalysis was benefited from the doping of InVO₄, which reduced the wide intrinsic band gap and improved the absorption and utilization ability of visible light. Meanwhile, a dual Z-scheme heterostructure interface was constructed to realize the rapid separation of photogenerated electron-hole pairs. This investigation may provide referential significance for the exploration and fabrication of new and efficient g-C₃N₄-based heterostructure.

1 Introduction

Nowadays, rapid industrialization growth discharges a large number of non-biodegradable pollutants, causing great harm to the ecological environment.

Especially in the manufacturing process of textile industry, 10–50% of printing and dyeing wastewater containing complex aromatic structure will be produced [1]. Therefore, how to effectively degrade printing and dyeing wastewater is one of the most

Address correspondence to E-mail: liyuzhen@tyut.edu.cn; chenwenjun1979@126.com

urgent problems to be solved in wastewater treatment. At present, technologies have been reported to remove organic pollutants from wastewater, such as photocatalytic technology, membrane filtration, reverse osmosis, and adsorption [2, 3]. Among different technologies, semiconductor photocatalysis is considered as an efficient, environmental-friendly and low-cost treatment method to degrade contaminants, and its photocatalytic function is attributed to the light-induced generation of charge carrier pairs which can transfer to the surface of the material and exhibit unique redox properties [4, 5]. However, traditional photocatalysts, such as pure TiO_2 , cannot be fully applied to photocatalysis field due to its broad band gap (about 3.2 eV) only responding in the ultraviolet region and high photoelectron-hole compound rate [6, 7]. Therefore, in order to enhance the utilization rate of sunlight, it has great significance to develop new photocatalysts with superior visible light response.

The emerging graphite-like phase carbon nitride ($\text{g-C}_3\text{N}_4$) material is a polymeric layered semiconductor with defect-rich N-bridged tri-s-triazine or s-triazine as the basic structural unit. Generally, $\text{g-C}_3\text{N}_4$ has been widely used as a material for photocatalytic treatment of pollutants due to its simple preparation method, stable physical and chemical properties, and suitable optical band gap (about 2.7 eV) [8–10]. Nevertheless, the certain deficiencies of $\text{g-C}_3\text{N}_4$, including inadequate sunlight absorption ability, low photo response current, and high photoinduced electron–hole pairs composite rate, result in poor photocatalytic efficiency [11, 12]. To overcome the above defects, Zhou et al. have summarized a series of strategies including heteroatom doping, structure modification, shape-control synthesis, semiconductor coupling, and dye-sensitization to improve the photocatalytic activity of $\text{g-C}_3\text{N}_4$ [13]. In recent years, coupling it with the different types of semiconductor materials, such as metal oxides, metal sulfides, oxometallates, and bismuth oxyhalides [14–18], to fabricate II type or Z-scheme heterojunction, is an effective way to enhance the photocatalytic efficiency by broadening the light response range and prolonging the lifetime of the photoinduced charge carriers [19, 20]. Especially, Z-scheme heterojunction is helpful to maintain the superior redox ability of electrons and holes after charge transfer [21]. Moreover, many researchers are devoted to constructing

ternary heterojunctions to further improve the photocatalytic performance of catalytic materials [22, 23].

Nanocomposite photocatalysts have been attracted much research attention because of their comprehensive advantages and synergistic effects which contributes to the separation of photogenerated electrons and holes. [24, 25]. As a typical layered semiconductor, Bi_2S_3 is endowed with a direct band gap of about 1.2–1.7 eV [26]. The narrow band gap is the direct advantage of choosing Bi_2S_3 as photocatalyst. Bi_2S_3 was successfully loaded onto $\text{g-C}_3\text{N}_4$ by ultrasonic method [27] and one-pot method [28], which can enhance the absorption of visible light and provide energy for the rapid transfer of photogenerated carriers, thus showing excellent photocatalytic performance. In addition, narrow band gap semiconductor InVO_4 ($E_g = 2.3$ eV) is also an important visible-driven catalytic material due to its high visible light utilization rate, adjustable morphology and size, and simple synthesis method [29]. Studies have shown that the energy levels of $\text{g-C}_3\text{N}_4$ and InVO_4 are well matched overlapping band structures [30]. Therefore, it is predicted that the introduction of InVO_4 in $\text{Bi}_2\text{S}_3/\text{g-C}_3\text{N}_4$ Z-scheme system could construct dual Z-scheme heterojunction, which further expands the reduction or oxidation surfaces to improve the photocatalytic performance [31].

In order to further analyze the optical response and light catalytic properties of $\text{g-C}_3\text{N}_4$ -based composites, on the basis of $\text{Bi}_2\text{S}_3/\text{g-C}_3\text{N}_4$, ternary dual Z-scheme $\text{InVO}_4/\text{Bi}_2\text{S}_3/\text{g-C}_3\text{N}_4$ heterojunctions were firstly synthesized in this work. The crystal structure, micromorphology, chemical composition, and optical properties of the ternary photocatalyst were analyzed by means of various characterization methods. The photocatalytic activity was measured by degradation of anion dye Reactive Blue 19 (RB19), and the photocatalytic degradation mechanism was explored by free radical capture experiment. In comparison with pure $\text{g-C}_3\text{N}_4$, InVO_4 and $\text{Bi}_2\text{S}_3/\text{g-C}_3\text{N}_4$, the as-prepared $\text{InVO}_4/\text{Bi}_2\text{S}_3/\text{g-C}_3\text{N}_4$ composites displayed higher visible light absorption efficiency, stronger catalytic activity, and better stability. With the optimal content of 5 wt% InVO_4 in the composite, 5wt% $\text{InVO}_4/\text{Bi}_2\text{S}_3/\text{g-C}_3\text{N}_4$ performed the excellent visible light catalytic activity for the degradation of RB19, and the degradation rate of RB19 (15 mg/L) could reach 97% after 100 min of visible light irradiation. To prove the advantages of $\text{InVO}_4/\text{Bi}_2\text{S}_3/\text{g-C}_3\text{N}_4$, Table 1 presents a retrospective analysis using

multiple photocatalysts for earlier studies on the degradation of dye under visible light.

2 Experimental section

2.1 Chemicals and materials

Urea (H_2NCONH_2 , 99%) and melamine ($\text{C}_3\text{H}_6\text{N}_6$, 99%) were bought from Tianjin Damao Chemical Reagent Factory (China). $\text{Bi}(\text{NO}_3)_3 \cdot 5\text{H}_2\text{O}$ (99%) was obtained from Tianjin Kaitong Chemical Reagent Co., Ltd. $\text{Na}_2\text{S}_2\text{O}_3 \cdot 5\text{H}_2\text{O}$ (99%) was provided from Tianjin Guangfu Technology Development Co., Ltd. $\text{InCl}_3 \cdot 4\text{H}_2\text{O}$ (99%) and NH_4VO_3 (99%) were from Tianjin Jinke Fine Chemical Research Institute. RB19 was purchased from Shanghai Maclean Biochemical Technology Co., Ltd. P-benzoquinone (BQ, 99%) was from Tianjin Qinghua Jinying Technology Co., Ltd. Tert-butanol (TBA, 99%) came from Tianjin Beichen Founder Reagent Factory. Ammonium oxalate (AO, 99%) was from Tianjin Zhiyuan Chemical Reagent Co., Ltd. Nitrotetrazolium Blue chloride (NBT) was from Hefei BSF Biology Science and Technology Co., Ltd. In this research, all of the materials were analytical grade without further purification. In addition, distilled water was used during the whole experiment process.

2.2 Catalyst preparation

2.2.1 Preparation of $\text{Bi}_2\text{S}_3/\text{g-C}_3\text{N}_4$

Pure $\text{g-C}_3\text{N}_4$ was prepared by calcining urea and melamine at high temperature [36]. Typically, 10.5 g urea and 4.5 g melamine were added to a covered alumina crucible and placed in a muffle furnace for 4 h at 550 °C, in which heating rate is 5 °C/min. After cooling to room temperature, the obtained light

yellow $\text{g-C}_3\text{N}_4$ was ground into powder for further use.

Bi_2S_3 was prepared by a wet-impregnation method [37]. Firstly, 1.9403 g $\text{Bi}(\text{NO}_3)_3 \cdot 5\text{H}_2\text{O}$ and 0.7445 g $\text{Na}_2\text{S}_2\text{O}_3 \cdot 5\text{H}_2\text{O}$ were uniformly dissolved in 50 mL methanol by ultrasonication for 10 min, and then stirred on a magnetic agitator for 60 min. Then, the suspension was transferred into a 100-mL polytetrafluoroethylene-lined stainless autoclave, heated at 180 °C for 12 h. Finally, the products were cooled to room temperature naturally, collected by centrifugation, and washed with anhydrous ethanol, distilled water for 3 times, and fully dried in an oven at 60 °C to obtain the grassy black Bi_2S_3 sample.

$\text{Bi}_2\text{S}_3/\text{g-C}_3\text{N}_4$ composite was synthesized by a simple wet-impregnation and calcination. In detail, 1 g $\text{g-C}_3\text{N}_4$ was dispersed in 80 mL methanol and treated with ultrasonic for 30 min to obtain solution A. Then, Bi_2S_3 with a mass doping ratio of 5% was dissolved in $\text{g-C}_3\text{N}_4$ solution, and the solution B was obtained after ultrasonic treatment for 60 min. Then, A and B were mixed through magnetic stirring for 24 h. After the reaction, the product was dried at 60 °C and finally calcined at 250 °C for 3 h. After grinding, the light yellow powdery photocatalyst of $\text{Bi}_2\text{S}_3/\text{g-C}_3\text{N}_4$ was collected and denoted as 5BS/CN.

2.2.2 Preparation of $\text{InVO}_4/\text{Bi}_2\text{S}_3/\text{g-C}_3\text{N}_4$

$\text{InCl}_3 \cdot 4\text{H}_2\text{O}$ and NH_4VO_3 were used to fabricate bare InVO_4 . Usually, 0.0638 g $\text{InCl}_3 \cdot 4\text{H}_2\text{O}$ and 0.0255 g NH_4VO_3 were dissolved in 50 mL distilled water. Subsequently, the NaOH solution was added dropwise to the above mixture and the pH was adjusted to 6–8. The InVO_4 was obtained by ultrasonic for 30 min.

A series of $\text{InVO}_4/\text{Bi}_2\text{S}_3/\text{g-C}_3\text{N}_4$ hybrid with different doping ratios of InVO_4 (denoted as $x\text{V}/5\text{BSCN}$, $x = 3, 5, 10, 15$, and 20 wt% with x representing the

Table 1 Comparison of the photocatalytic degradation efficiency

Photocatalyst	Pollutant	Conc. (mg/L)	Dosage (g/L)	Time (min)	Removal (%)	Light source	Refs
$\text{InVO}_4/\text{Bi}_2\text{S}_3/\text{g-C}_3\text{N}_4$	RB19	15	0.8	100	97	300w XL	This work
$\text{g-C}_3\text{N}_4\text{-ZnO}/\text{Cu}_2\text{O}$	RhB	50	0.5	100	91	500w XL	[32]
$\text{g-C}_3\text{N}_4/\text{ZnO}$	MB	6	1.5	120	95	100w HL	[33]
$\text{g-C}_3\text{N}_4/\text{Bi}_4\text{Ti}_3\text{O}_{12}$	RhB	5	5	150	67	200w XL	[34]
BaTiO_3/GO	MB	5	0.5	300	95	500w XL	[35]

XL xenon lamp, HL halogen lamp, RhB rhodamine B, MB methylene blue

weight percentage of InVO₄) were synthesized by the following method. 1 g 5BS/CN uniformly dispersed in 80 mL distilled water by ultrasonication for 10 min. Then, a certain amount of InVO₄ was added into the above suspension. Next, the mixture was continued to be sonicated for 30 min and further magnetic stirred for 24 h at room temperature. Finally, ternary InVO₄/Bi₂S₃/g-C₃N₄ photocatalyst was fully dried at 60 °C and collected by ground.

2.3 Catalyst characterization

The phase purity and crystal structure information were determined by X-ray diffraction measurement (XRD) (LABXRD-6000) using Cu-K α source ($\lambda = 0.154$ nm) with a step size of 0.02° in the range of 10°–80° at the scan rate of 2°/min at 30 mA and 40 kV. The functional groups and chemical bonds were qualitative analyzed by Fourier transform infrared (FT-IR) spectra on thermo Scientific Nicolet iS10 spectrometer taking KBr as the reference in the range of 500–4000 cm⁻¹. The morphologies of the photocatalysts were observed. The morphologies and microstructures of the samples were investigated by the transmission electron microscopy (TEM) (JEM-2500SE) at 200 kV and the field emission scanning electron microscopy (FE-SEM) (JSM-7100F) at 15 kV. Energy dispersive X-ray spectroscopy (EDS) attached to SEM was used to determine the chemical composition of the composite. N₂ adsorption and desorption isotherms at -196 °C were obtained using a Micromeritics ASAP 2020. The BET (Brunauer–Emmett–Teller) method and BJH (Barrett–Joyner–Halenda) method were used to calculate the specific surface area and pore size distribution, respectively. The absorption edge of the catalysts was measured by UV–Vis diffuse reflectance spectra (UV–Vis DRS) (Hitachi U-3900, Japan) using Ba₂SO₄ as the background in the range from 200 to 800 nm. The catalysts photoluminescence (PL) spectra were recorded on a Shimadzu RF-6000 fluorescence spectrophotometer with slit width of 3 nm in the range from 400 to 700 nm at the scan rate of 6000 nm/min. The photocurrent response and electrochemical impedance spectroscopy (EIS) were measured in Na₂SO₄ (0.1 M) electrolyte solution by Chi660E electrochemical workstation with a three-electrode cell, and the platinum electrode, ITO glass (25 × 15 × 1.1 mm) which was coated by the samples, Ag⁺/AgCl electrode were

used as counter electrode, working electrode, and reference electrode, respectively.

2.4 Catalytic experiments

The photocatalytic activities were evaluated by the degradation of RB19 under visible light irradiation. The visible light source was a 300 W Xenon lamp (CEL-HXF300) equipped with a 420 nm cutoff filter, 15 A current, and 14 V voltage. Typically, 200 mg of photocatalysts with different mass ratios of InVO₄ was added to a 250 mL 20 mg/L of RB19 dyes solution and then placed in a 300 mL glass reactor. Before the irradiation reaction, the above suspension was firstly dispersed by ultrasound for 10 min and then stirred in the dark for 40 min to establish an adsorption–desorption equilibrium. Afterward, the suspension was placed under visible light in the photocatalytic chamber for 100 min. To eliminate the effect of temperature, the reaction vessel was endowed with a large beaker containing an appropriate amount of cold water (25 ± 1 °C). Meanwhile, 10 mL of photoreacted solution was sampled at regular irradiation time intervals (20 min) and centrifuged twice for 5 min each (10,000 rpm). Lastly, the concentration of RB19 was tested on a UV-1800PC spectrophotometer (MAPAD, Shanghai, China) ($\lambda_{\max} = 594$ nm). The photocatalytic efficiency (η) was calculated according to the following formula:

$$\eta = \frac{C}{C_0}, \quad (1)$$

where C_0 is the initial concentration of RB19 dyes solution and C is the real-time concentration of RB19 dyes solution during the reaction. Furthermore, the first-order rate constant k_{obs} of the photocatalytic process is measured by the following formula [38]:

$$k_{\text{obs}} = -\frac{1}{t} \ln \left(\frac{C}{C_0} \right), \quad (2)$$

where k_{obs} (min⁻¹) is the first-order rate constant, C_0 is the RB19 dyes concentration after 40 min dark adsorption (mg/L), and C is the instantaneous concentration of the RB19 solution at illuminated time t (min).

In addition to the experiment of optimal xV/BSCN doping ratio, the influence of catalyst dosage, initial concentration of RB19, initial pH, and the stability of the photocatalyst were also studied. The

photocatalytic properties of $xV/5BSCN$ were explored from different perspectives.

2.5 Reactive species experiments

2.5.1 Active species trapping experiments

In order to explore the reaction mechanism and determine the generation of main active species in the process of the photocatalytic degradation of RB19, 2 mL TBA, 0.0621 g AO, and 0.0054 g BQ quenchers were used as scavengers of hydroxyl radicals ($\cdot OH$), photo-holes (h^+), and superoxide radicals (O_2^-), respectively, were added to the reaction system after the adsorption–desorption equilibrium, and the remaining steps were the same as for other degradation experiments.

2.5.2 NBT transformation experiments

NBT was often used to quantitatively analyze the O_2^- in photocatalytic reaction [39]. Briefly, 50 mg as-prepared catalysts were dispersed in 250 mL distilled water by ultrasonication for 10 min. Next, 10.2205 mg NBT was added in the above dispersion to react. After a given time interval, the concentration of NBT was measured with recording variations of the absorption band maximum (259 nm) in the UV–Vis spectra to react with the amount of O_2^- .

3 Results and discussion

3.1 Optimal doping ratio selection

Figure 1a and b shows the photodegradation efficiency of 25 mg/L RB19 and the first-order rate constants of each reaction over the $g-C_3N_4$, $InVO_4$ (V), 5BS/CN, and the ternary catalysts with different $InVO_4$ doping ratios. It could be clearly seen from Fig. 1a that the adsorption capacity of $g-C_3N_4$ to RB19 solution was larger, reaching 41.2%, and the photocatalytic degradation rate of RB19 solution under visible light was lower and degraded to 85.3% after 100 min of light exposure. Pure $InVO_4$ had no adsorption and degradation ability at all. The binary catalyst 5BS/CN improved the degradation capacity of pure $g-C_3N_4$ to 91.2% after 100 min of visible light irradiation. The photocatalytic performance of 5BS/CN was further increased by doping $InVO_4$.

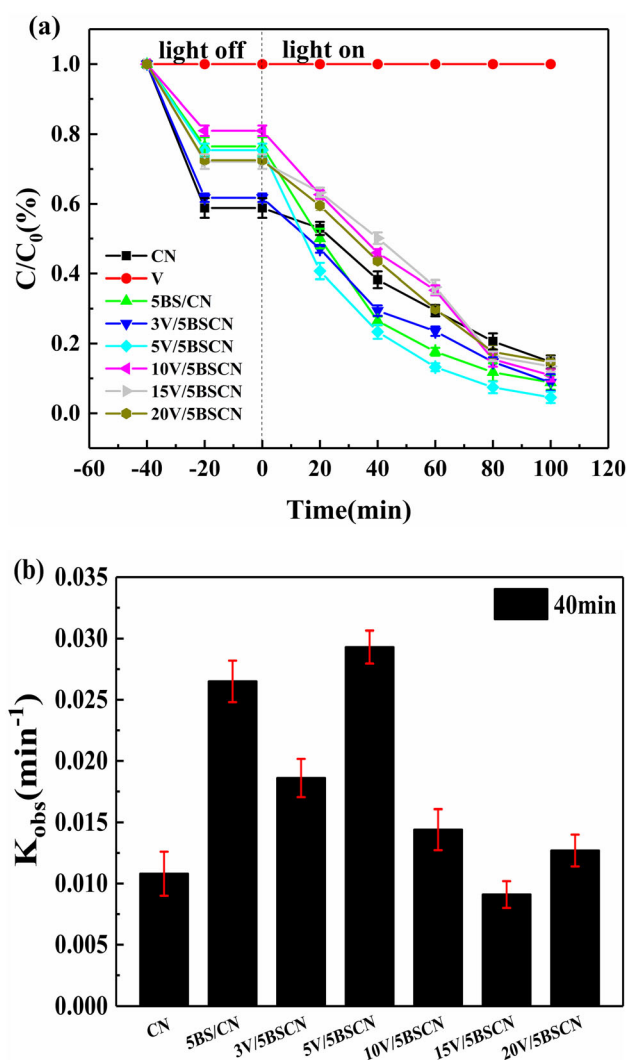


Fig. 1 a Photocatalytic comparison of $xV/5BSCN$ for different $InVO_4$ doping ratios and b first-order rate constants (the dosage of catalyst = 1.0 g/L, C_{RB19} = 25 mg/L, pH 7.0)

Obviously, the catalytic activity of the $xV/5BSCN$ composites was closely related to their doping ratios. The photocatalytic rates of 3 V/5BSCN, 5 V/5BSCN, 10 V/5BSCN, 15 V/5BSCN, and 20 V/5BSCN were 91.2%, 95.5%, 89.1%, 86.6%, and 85.3%. Clearly, as the doping ratio of $InVO_4$ increased from 3 to 5%, the photodegradation efficiency increased gradually; however, when the loading percent of $InVO_4$ further increased from 5 to 20%, the photocatalytic rate for RB19 tended to a significant decrease. It indicated that 5 V/5BSCN had the best photocatalytic activity. This might be due to excessive $InVO_4$ deposition, which was not well dispersed on the surface of the material, affecting its absorption of light, reducing the number of effective heterogeneous junctions in

the composite material, and influencing charge transfer between heterogeneous junction interfaces [30]. Similarly, the first-order rate constant of 5 V/5BSCN also was the largest at 40 min. Therefore, the 5 V/5BSCN were selected as the optimal photocatalyst for the following studies.

3.2 Characterization

3.2.1 Structure and morphology

The crystal structure of as-synthesized $g\text{-C}_3\text{N}_4$, Bi_2S_3 , InVO_4 , 5BS/CN, 5 V/5BSCN were detected by XRD pattern and are shown in Fig. 2. Obviously, two diffraction peaks of pure $g\text{-C}_3\text{N}_4$ were observed at 13.02° and 27.52° corresponding to (100) and (002) planes of pristine $g\text{-C}_3\text{N}_4$ (JCPDS 87-1526), which were derived from the tri-s-thiazine units and the stacking of the conjugated aromatic systems, respectively [40, 41]. The crystal structures of bare Bi_2S_3 were orthorhombic crystal structure and their diffraction peaks at 23.44° , 29.1° , 31.94° , 45.56° , 52.46° , and 62.40° could be indexed to (130), (211), (221), (002), (351), and (152) crystal planes respectively, which matched well with the standard card (JCPDS 17-0320) [42, 43]. In the XRD pattern of 5BS/CN, the diffraction peaks of $g\text{-C}_3\text{N}_4$ and Bi_2S_3 appeared simultaneously, which indicated the successful loading of Bi_2S_3 without impurity. The XRD spectra of pure InVO_4 showed that the diffraction peaks at 19.8° , 21.5° , 31.8° , 33.0° , 41.6° , 51.0° , and 60.9° could

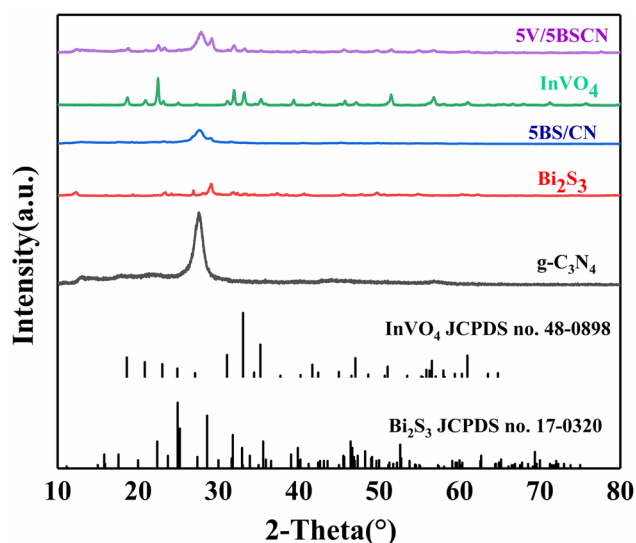


Fig. 2 XRD patterns of $g\text{-C}_3\text{N}_4$, Bi_2S_3 , 5BS/CN, InVO_4 and 5 V/5BSCN

be ascribed to (110), (020), (200), (112), (202), (042), and (242) crystal planes of orthorhombic phase InVO_4 (JCPDS. No 48-0898), [44]. With the addition of InVO_4 to 5BSCN, it could be found that the main diffraction peaks of InVO_4 and 5BS/CN existed at the same time in the XRD pattern of 5 V/5BSCN hybrid, which illustrated the successful preparation of the ternary photocatalysts. Furthermore, the weak the characteristic peak intensity of InVO_4 in the composite might be due to the low content of InVO_4 .

The functional groups and bonds of $g\text{-C}_3\text{N}_4$, 5BS/CN, and 5 V/5BSCN were tested on the FT-IR spectra, the results of which are displayed in Fig. 3. It could be seen from Fig. 3 that the characteristic peaks of the three materials were mainly concentrated in the range of $500\text{--}3500\text{ cm}^{-1}$. In the FT-IR spectrum of $g\text{-C}_3\text{N}_4$, the sharp absorption band at 807 cm^{-1} was from the distinctive vibration of tri-s-triazine ring units [45], the absorption peaks in the range of $1200\text{--}1700\text{ cm}^{-1}$ were caused by stretching vibrations of C–N and C=N bonds [46]. A wide absorption band at 3250 cm^{-1} was the stretching vibrations of O–H and N–H due to the adsorption of water molecules and residue of amino groups on the surface of $g\text{-C}_3\text{N}_4$. In the FT-IR spectra of 5BS/CN, the absorption peaks at 3254 cm^{-1} and 811 cm^{-1} which also existed in the FT-IR spectra of pristine Bi_2S_3 , corresponding to the stretching vibrations of the residual N–H and Bi–S groups respectively [47], thus demonstrating the existence of Bi_2S_3 in 5BS/CN composite. The diffraction peak of 5 V/5BSCN appeared at 809 cm^{-1} owing to the interaction

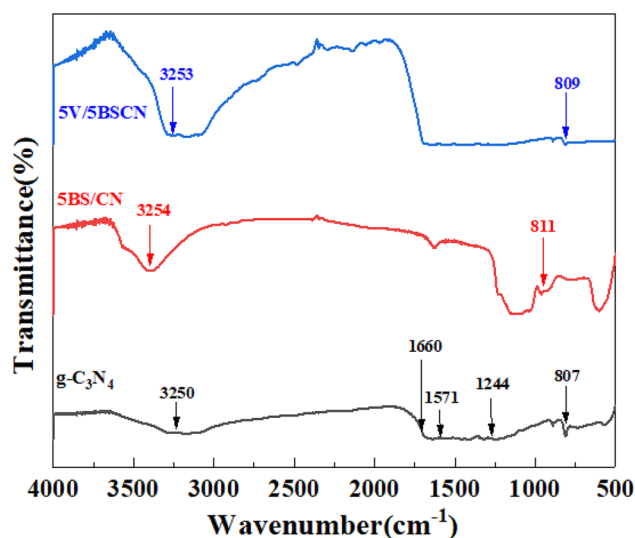


Fig. 3 FT-IR spectra of $g\text{-C}_3\text{N}_4$, 5BS/CN and 5 V/5BSCN

between tri-s-triazine ring units of g-C₃N₄ and Bi-S groups of Bi₂S₃, which also suggested the coexistence of g-C₃N₄ and Bi₂S₃. Moreover, the diffraction peak of 5 V/5BSCN at 3253 cm⁻¹ was due to the stretching vibrations of N-H. However, no characteristic peaks of InVO₄ could be observed in the pattern of 5 V/5BSCN, which might be attributed to low amount of InVO₄ loading on 5BS/CN. In fact, the existence of InVO₄ in the nanocomposite could be further verified by TEM based on the recognition of the morphology and microstructure.

Figure 4 displays TEM images of g-C₃N₄, Bi₂S₃, 5 V/5BSCN, and HR-TEM images of 5 V/5BSCN. Figure 4a shows that the internal structure of g-C₃N₄ was layered and overlapped. And Fig. 4b presents that Bi₂S₃ had a rod-like structure. TEM image of 5 V/5BSCN (Fig. 4c) showed that the bar Bi₂S₃ and the irregular stacked layered g-C₃N₄ were uniformly covered with dark-colored flake substances, indicating that the InVO₄ was doped into the 5BS/CN composite material to form the ternary photocatalyst, which was consistent with the XRD analysis. In addition, Fig. 4d shows that the lattice spacing of the lattice stripes was 0.346 nm attributed to the (220) crystal plane of InVO₄ [48].

The distribution of InVO₄ in the 5 V/5BSCN composite was further demonstrated by elemental mapping. As shown in Fig. 5, C, N, O, S, Bi, In, and V elements were uniformly distributed within 5 V/5BSCN composite. Meanwhile, the weight percentages of each element in 5 V/5BSCN were detected in Fig. 5i, further implying the coexistence of InVO₄, Bi₂S₃ and g-C₃N₄ without other impurities.

The textural properties of pure g-C₃N₄ and 5 V/5BSCN were inferred from their N₂ adsorption-desorption isotherms (Fig. 6). All photocatalysts showed type-IV adsorption isotherms with H₃ type hysteresis loops, indicating the existence of slit-like pores created by the stacked nanosheets [49]. BET surface area for g-C₃N₄ and 5 V/5BSCN was 63.4485 m²g⁻¹ and 59.7659 m²g⁻¹, respectively. Compared to the pure g-C₃N₄, the composite materials delivered low surface area. The decrease in the surface area of g-C₃N₄ might be due to the fact that spherical InVO₄ dispersed on the surface of CN blocks the pores of CN. These results could be affirmed by the above-mentioned SEM. It was also a good explanation that the adsorption capacity of RB19 of composite material was lower than that of pure CN. Moreover, 5 V/

5BSCN showed more micropores (2 nm) that might be generated by stacked nanosheets.

3.3 Optical properties

The light harvesting capacities of g-C₃N₄, Bi₂S₃, InVO₄, and 5BS/CN, 5 V/5BSCN composites can be evaluated by UV-Vis diffuse reflectance (DRS) spectra. As shown in Fig. 7a, the optical absorption edges of g-C₃N₄, Bi₂S₃, and InVO₄ were 475, 1130, and 620 nm respectively, while the optical absorption edges of the doped composite materials 5BS/CN and 5 V/5BSCN were 485 and 680 nm, respectively. This indicated that the light absorption edges of the composites had red shift compared with that of pure g-C₃N₄, and the visible light absorption region was significantly broadened, thus improving the utilization efficiency of visible light.

The band gap energy (E_g) of photocatalysts can be calculated by the following Kubelka-Munk Eq. [50]:

$$\alpha hv = A(hv - E_g)^{\frac{n}{2}} \quad (3)$$

where α is the absorption coefficient, E_g is the band gap energy, A , h , and v are a proportionality constant, plank constant, and light frequency, respectively, the value of n depends on the type of optical transition of semiconductors ($n = 1$ for direct transition and $n = 4$ for indirect transition). According to the previous research, g-C₃N₄, Bi₂S₃ and InVO₄ are all direct semiconductors, so the value of n is 1 for them [41, 44, 51]. According to the plots of $(\alpha hv)^{1/2}$ versus hv (Fig. 7b), the calculated E_g values of g-C₃N₄, Bi₂S₃ and InVO₄ were 2.74, 1.90, and 2.34 eV respectively. After the introduction of Bi₂S₃, the band gap of 5BS/CN composites was 2.25 eV, which was 0.49 eV smaller than that of pure g-C₃N₄. Moreover, InVO₄ was further introduced, the band gap of the 5 V/5BSCN was continuously reduced to 1.96 eV. This indicated that heterogeneous junctions were constructed between g-C₃N₄, Bi₂S₃ and InVO₄, which effectively reduced the interface contact barrier, strengthened the electron coupling between semiconductors, and thus enhanced the photocatalytic activity [52]. In addition, the valence band (VB) and conduction band (CB) of semiconductors can be calculated by the following formula [50]

$$E_{CB} = X - E^{\circ} - 0.5E_g \quad (4)$$

$$E_{VB} = E_{CB} + E_g \quad (5)$$

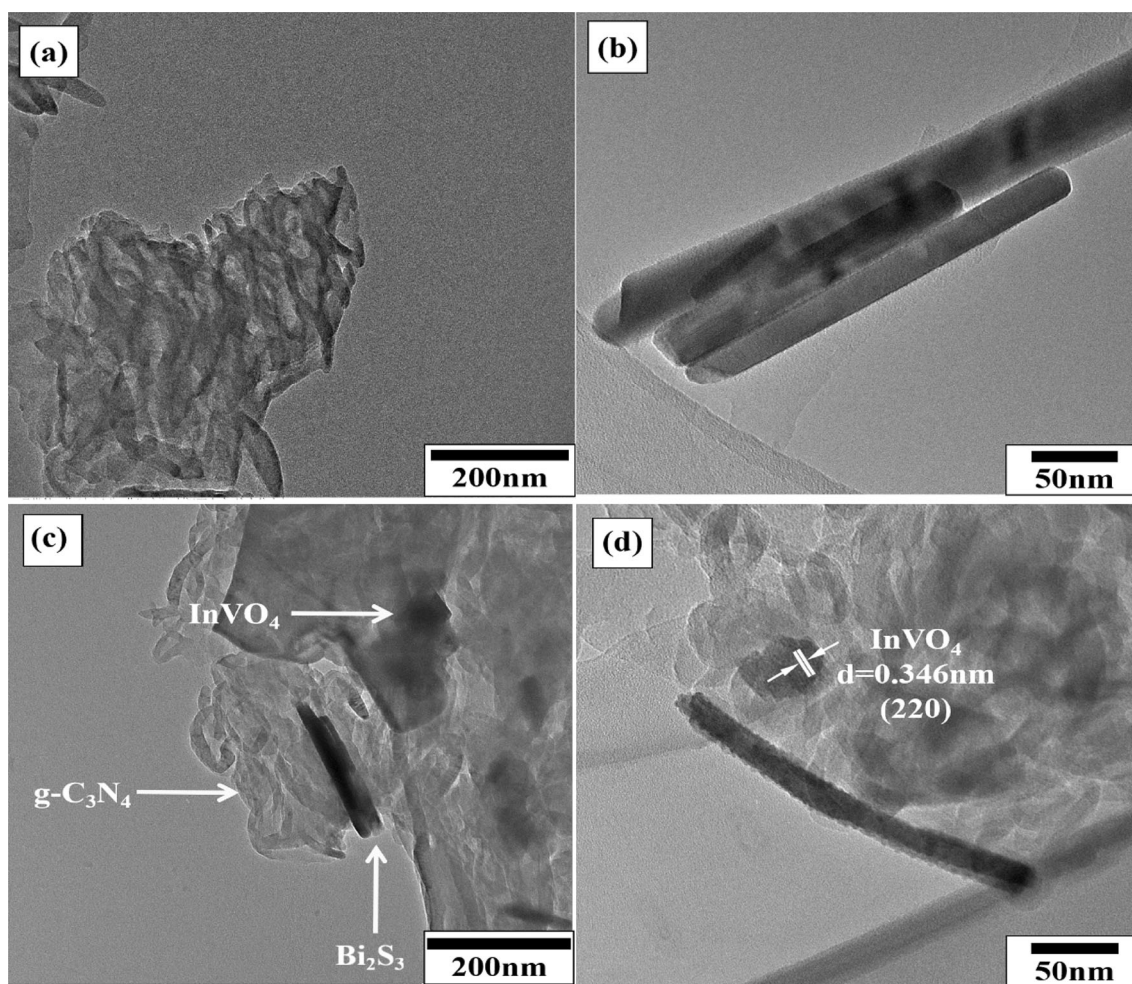


Fig. 4 TEM images of **a** $g\text{-C}_3\text{N}_4$, **b** Bi_2S_3 , **c** 5 V/5BSCN and HR-TEM images of **d** 5 V/5BSCN

where E_{VB} and E_{CB} are the valence band potential and conduction band potential of semiconductors. X is the electronegativity of the semiconductor, which is the geometric average value of the electronegativity of constituent atoms, and the X values of $g\text{-C}_3\text{N}_4$, Bi_2S_3 , and InVO_4 are 4.67, 5.56, and 5.03 eV, respectively [53–55]. E^e is the energy of free electrons on the hydrogen scale (about 4.5 eV). Using the Eqs. (4, 5), the VB edge potentials of $g\text{-C}_3\text{N}_4$, Bi_2S_3 , and InVO_4 were 1.54 eV, 2.01 eV, and 1.70 eV, respectively, and the CB edge potentials of them were -1.20 eV, -1.11 eV, and -0.64 eV, respectively.

3.4 Photocatalytic activities

3.4.1 Effect of catalyst dosage

In order to explore the effect of the photocatalyst dosage on degradation of RB19, the dosage gradient

of 5 V/5BSCN was set at 0.4, 0.6, 0.8, 1.0, and 1.2 g/L. Accordingly, the degradation rate of 25 mg/L RB19 and the first-order rate constant under 40 min illumination were studied, as shown in Fig. 8. Obviously, with the increase of the catalyst dosage, the adsorption capacity of the dark reaction was augmented, and when the catalyst dosage reached the maximum of 1.2 g/L, the dark adsorption capacity of RB19 achieved the maximum of 38.16% accordingly. This was because physical adsorption occurred during the dark reaction, in which the more the catalyst, the more the pollutant molecules were adsorbed. Figure 8a exhibits that the final degradation rate of RB19 also increased with the increase of dosage, which was 39.05%, 47.66%, 95.46%, 97.34%, and 97.42% respectively. Remarkably when the dosage of 5 V/5BSCN increased from 0.6 to 0.8 mg/L, the degradation rate increased significantly, and then the dosage further increased to 1.2 mg/L, the

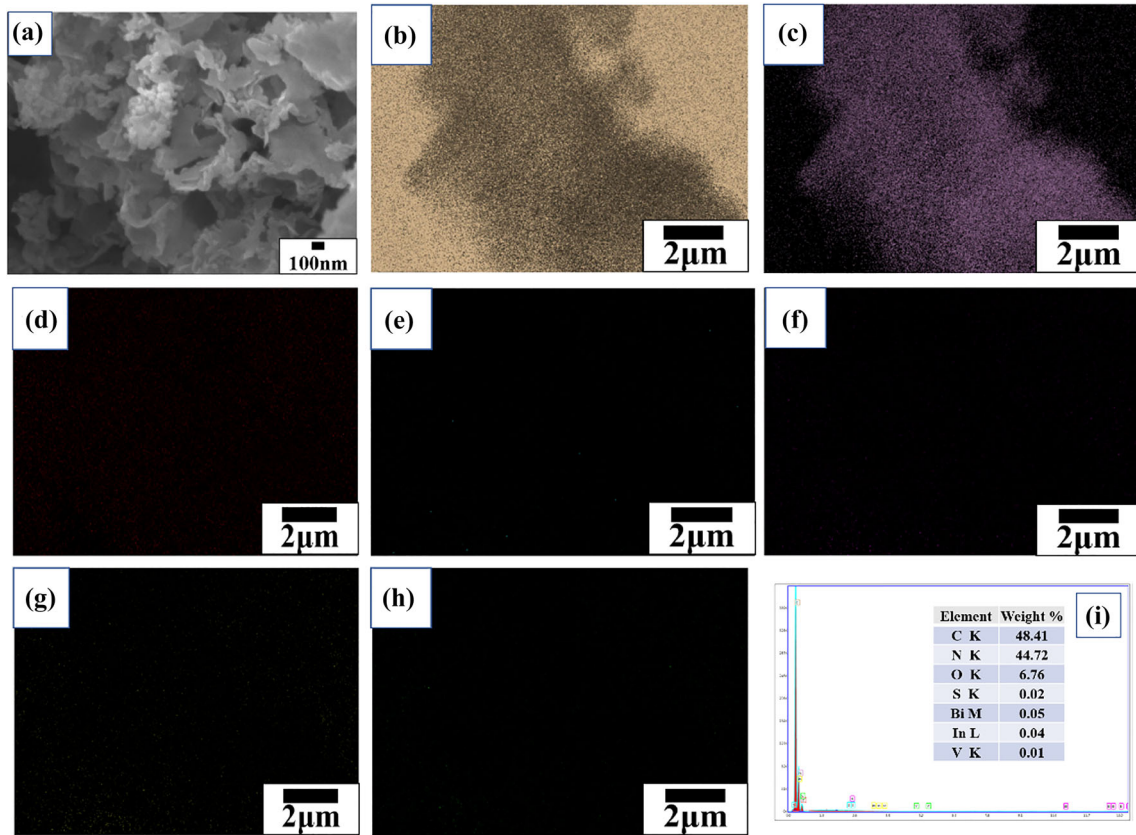


Fig. 5 a SEM image of 5 V/5BSCN, and EDX layered images of b C, c N, d O, e S, f Bi, g In, h V and i EDX spectrum of 5 V/5BSCN

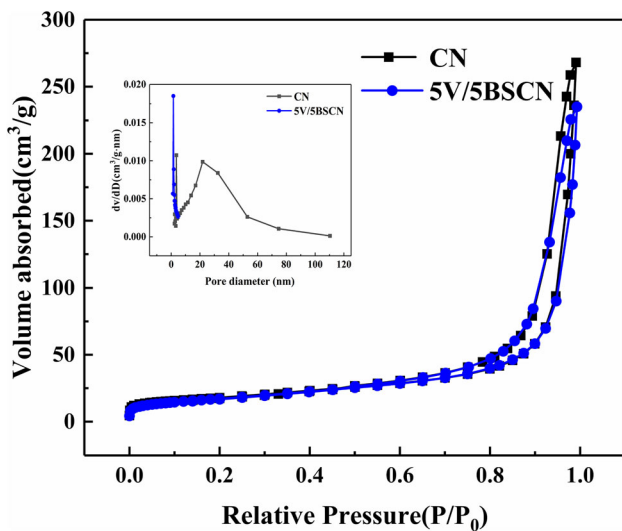


Fig. 6 BET surface area and the corresponding BJH pore size distribution curves (inset) of pure g-C₃N₄ and 5 V/5BSCN composite

degradation rate increased slowly. It could be seen from Fig. 8b that the rate constants corresponding to the dosage were 0.351×10^{-2} , 0.580×10^{-2} ,

2.931×10^{-2} , 2.905×10^{-2} , and $2.884 \times 10^{-2} \text{ min}^{-1}$, which showed a trend similar to that of degradation rate. This illustrated that an appropriate amount of catalyst could significantly improve the photocatalytic degradation efficiency, but increasing the amount of catalyst further had little effect on the degradation of pollutants and could even inhibit the process. This was because a small amount of the catalyst did not produce enough active charge carriers to afford excess amount of RB19 molecules, with the increase of its dosage, the more active sites could be contributed to enhance light utilization efficiency [56]. Nevertheless, when catalyst dosage surpassed a certain amount, the light transmittance began lower down, so less light could be irradiated to the surface of photocatalysts, which reduced the generation of the photogenerated electrons and holes, eventually resulting in the decrease of photocatalytic efficiency [56, 57]. Therefore, 0.8 g/L was chosen as the optimal dosage for 5 V/5BSCN for subsequent exploratory experiments.

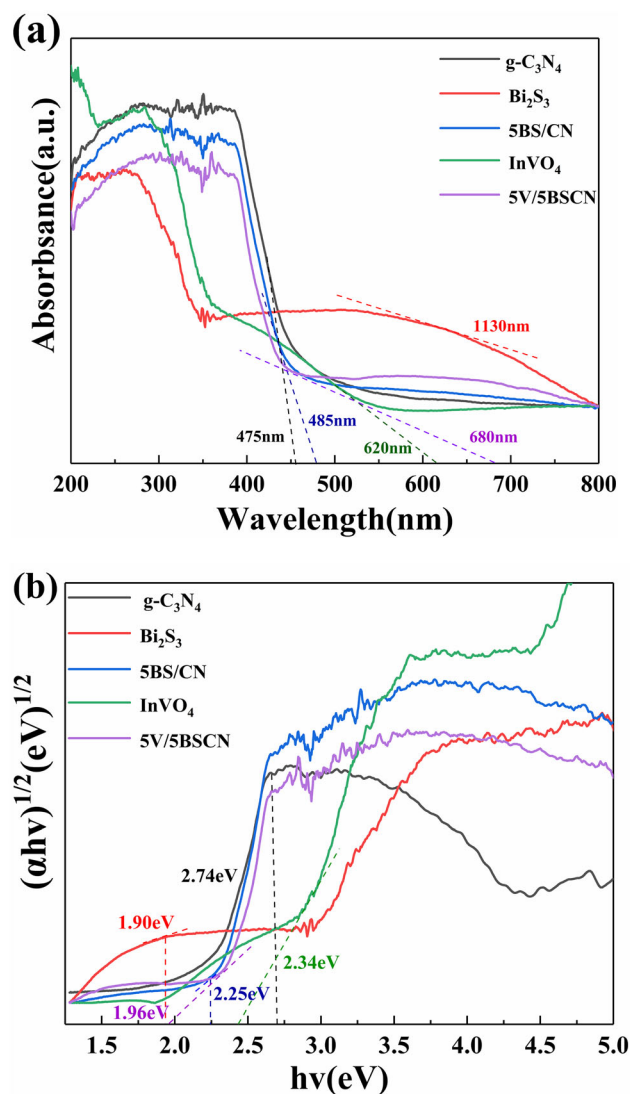


Fig. 7 a UV-Visible diffuse reflectance spectrum and b band gap diagram of g-C₃N₄, Bi₂S₃, 5BS/CN, InVO₄ and 5 V/5BSCN

3.4.2 Effect of initial concentration of RB19 solution

In order to investigate the effect of initial concentration of RB19 solution on degradation of RB19, the concentration gradient of RB19 was set at 10 mg/L, 15 mg/L, 20 mg/L, 25 mg/L, and 30 mg/L, and the dosage of 5 V/5BSCN was 0.8 g/L. As shown in Fig. 9, 5V/5BSCN degrading 15 mg/L and 25 mg/L RB19 performed better catalytic activity considering the dark adsorption capacity and degradation rate. And there was an inflection point when the initial concentration of the pollutant increased from 25 to 30 mg/L, the degradation rate decreased dramatically. The result indicated that RB19 solution of high concentration suppressed photocatalytic effect. This

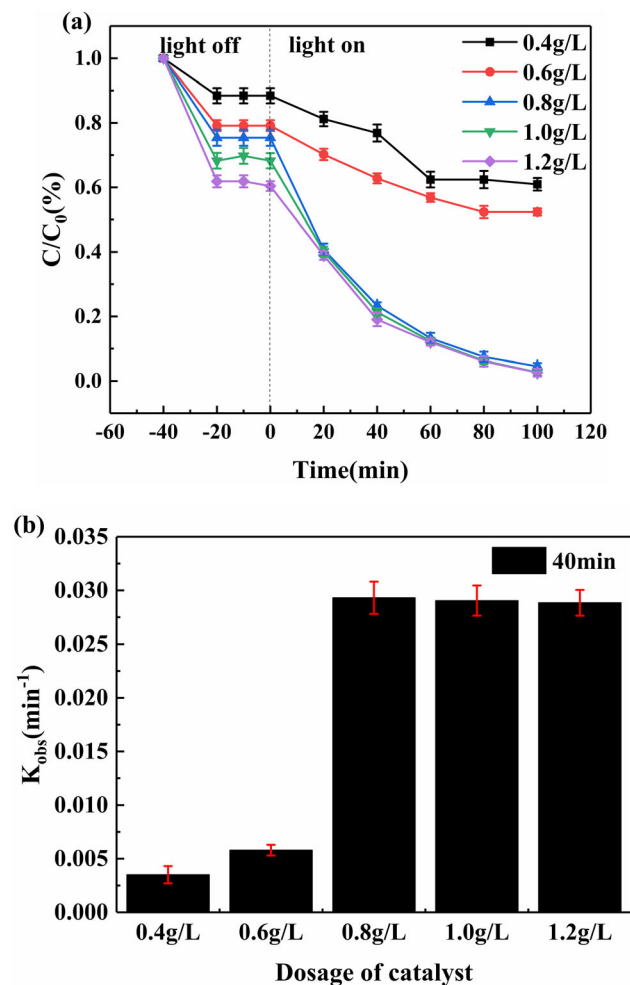


Fig. 8 a Effect of dosage on photocatalysis of 5 V/5BSCN and b first-order rate constants ($C_{RB19} = 25$ mg/L, pH 7.0)

was because with the increase of the concentration of RB19, the increasing adsorbed pollutants on the surface of the catalyst consumed photoelectron-hole pairs gradually which were hindered to recombination, thus showing a high degradation rate. When the concentration of pollutant solution reached to a high level certainly, on the one hand, the massive sedimentary of RB19 molecules reduced the visible light transmittance; on the other hand, the intermediate by-products that cannot be decomposed in time competed with pollutant molecules for active sites, retarding the reaction, thus leading to the reduction of photocatalytic efficiency [57]. Figure 9b shows that when the initial concentration of RB19 was 15 mg/L, the corresponding first-order rate constant presented a maximum value. So, 15 mg/L was the most suitable initial concentration of RB19 solution among them.

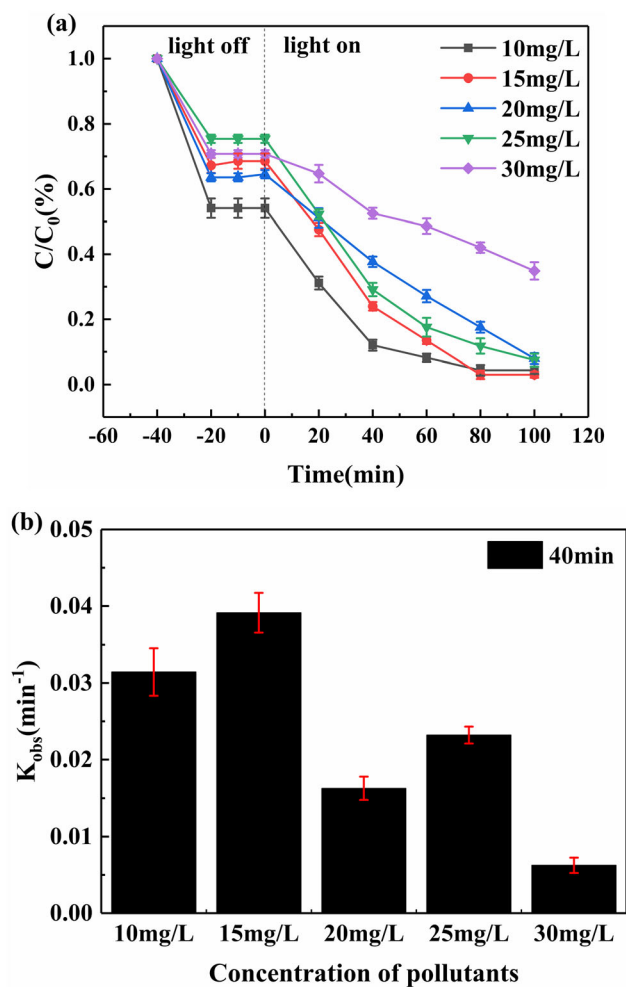


Fig. 9 **a** Effect of different concentrations on photocatalysis of 5 V/5BSCN and **b** first-order rate constants (the dosage of catalyst = 0.8 g/L, pH 7.0)

3.4.3 Effect of initial pH

In order to study the effect of the initial pH of the reaction solution on degradation of RB19, the photocatalytic degradation efficiency of RB19 was tested by 10ABCN at initial pH 3, 5, 7, 9, and 11. The initial concentration of RB19 was 15 mg/L, and the dosage of 5 V/5BSCN was 0.8 g/L. Figure 10 presents that the dark adsorption capacities of RB19 at the initial pH of 3, 5, 7, 9, and 11 were 92.17%, 48.50%, 25.93%, 25.93%, and 31.46%, respectively. It manifested that the higher the acidity, the greater the adsorption capacity, because pH affected the electronegativity of the catalyst [50, 58]. Under acidic conditions, the surface of the catalyst was positively charged, while RB19 was a negatively charged anionic dye, then the electrostatic attraction occurred between the

photocatalysts and pollutants giving rise to a plentiful adsorption of RB19 molecules on the surface of 5 V/5BSCN. On the contrary, in the alkaline environment, the surface of the catalyst was negatively charged, so there was electrostatic repulsion with the negatively charged RB19, which led to the weakening of the adsorption capacity of 5 V/5BSCN. As for the degradation effect, the degradation trend performed faster under alkaline conditions, especially when pH 11. This was because O₂ adsorbed on the surface of the catalyst reacted with the negative charge on the surface to generate active species ·O₂⁻ [59], then RB19 was rapidly degraded. However, after 40 min of photoreaction, the degradation rate of RB19 under alkaline conditions gradually slowed down, and the degradation under pH 11 reaction conditions almost stopped, mainly because the sulfur group of RB19 was substituted to form vinyl sulfone in alkaline environment and 2-hydroxyethyl sulfone [60], the stronger the basicity was, the stronger the substitution effect of the sulfur group was, thus slowing down the photocatalytic reaction process.

3.4.4 Stability experiment

The stability of 5 V/5BSCN was tested by photocatalytic degradation of RB19 in four cycles with the dye concentration of 15 mg/L. As shown in Fig. 11a, the degradation rate of RB19 decreased slightly after each cycle, reaching about 76% after 4 cycles, indicating that the 5 V/5BSCN composite material was relatively stable during photocatalytic degradation of

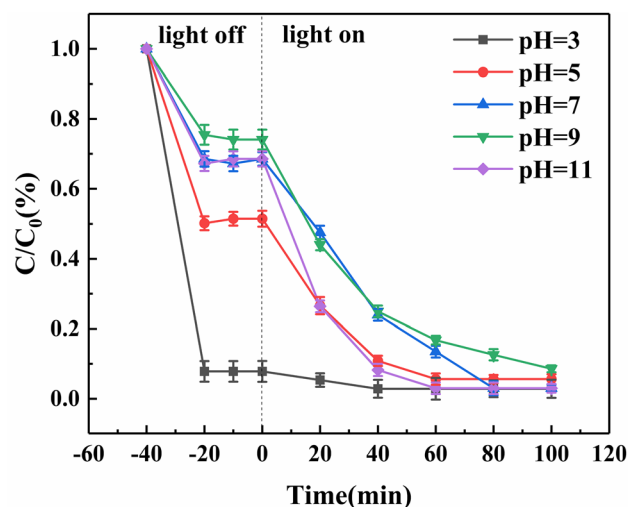


Fig. 10 Effect of initial pH on photocatalysis of 5 V/5BSCN (the dosage of catalyst = 0.8 g/L, C_{RB19} = 15 mg/L)

RB19 dyes. Moreover, XRD (Fig. 11b) and SEM (Fig. 11c, d) displayed that the crystal structure of 5 V/5BSCN heterojunction was not destroyed in the progress of the photocatalytic reaction. The stability might be due to the tight heterojunction interface conducive to the rapid separation of photogenerated electrons and holes.

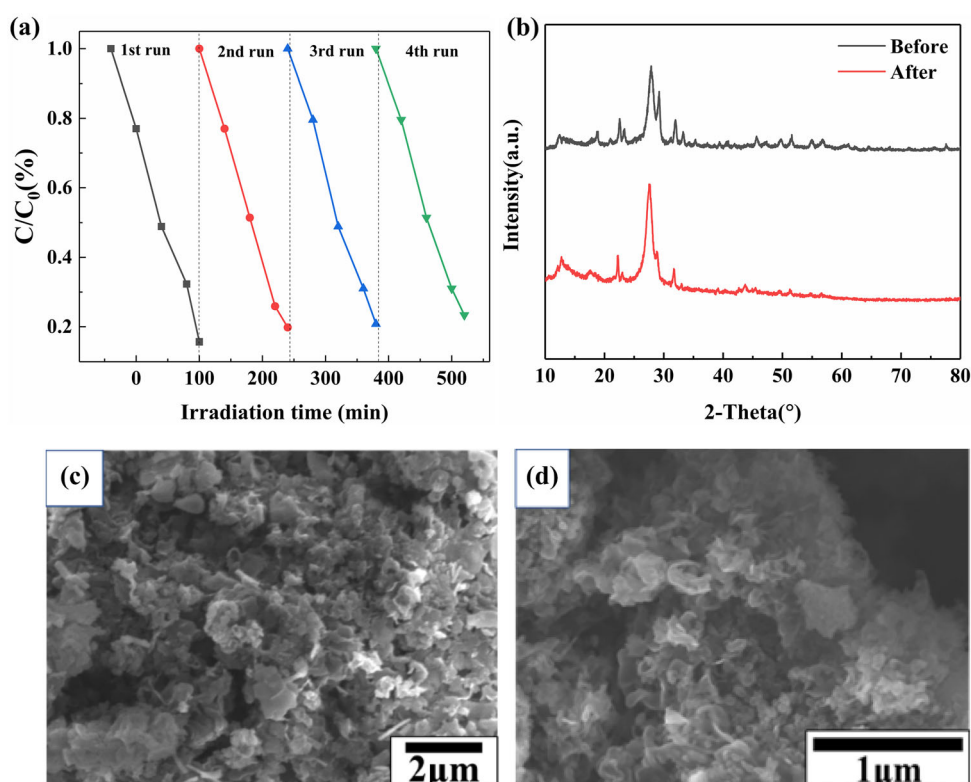
3.5 Photocatalytic mechanism

Fluorescence spectroscopy (PL) is an important method to study the photogenerated electron–hole separation ability. The stronger the peak of the fluorescence emission spectrum was, the higher the electron–hole recombination rate was [7, 61]. Figure 12 depicts the fluorescence spectra of pure $g\text{-C}_3\text{N}_4$, 5BS/CN, and 5 V/5BSCN. The PL spectrum of pure $g\text{-C}_3\text{N}_4$ had a strong emission peak caused by the band transition at 460 nm, which revealed that the electron–hole recombination rate was quite fast [62, 63]. Compared with pure $g\text{-C}_3\text{N}_4$, the PL peak of the 5BS/CN composite material was significantly weaker, illustrating that the construction of heterojunction could effectively inhibit the recombination of photogenerated carriers. Moreover, the PL peak of 5 V/5BSCN was further weaker, indicating that the

continuous loading of InVO_4 on the basis of 5BS/CN composite to construct a ternary heterojunction could further inhibit the recombination of photogenerated carriers and improve the photocatalytic degradation efficiency.

The photocurrent response and EIS further demonstrated the separation and transfer of photoinduced charge carriers. The photocurrent response of CN, 5BS/CN, and 5 V/5BSCN was monitored for several on–off cycles at open-circuit potential. Higher photocurrent density means a stronger carrier separation capacity [64]. As shown in Fig. 13a, the 5 V/5BSCN exhibited the highest photocurrent density, which were 2.3 and 2 times greater than $g\text{-C}_3\text{N}_4$ and 5BS/CN, respectively, indicating that 5 V/5BSCN had a higher carrier separation ability. The result of EIS is shown in Fig. 13b, the smaller the radius in EIS diagram was, the smaller the charge transfer resistance was at the electrode interface, suggesting the faster interfacial electron transport [65]. The EIS measurements revealed that the radius of Nyquist curve of 5 V/5BSCN was smaller than that of CN and 5BS/CN, and therefore, 5 V/5BSCN was proved to possess higher photogenerated charge transferability than pure CN.

Fig. 11 a Cyclic experiment, b XRD patterns, c, d SEM images of 5 V/5BSCN before and after photoreaction



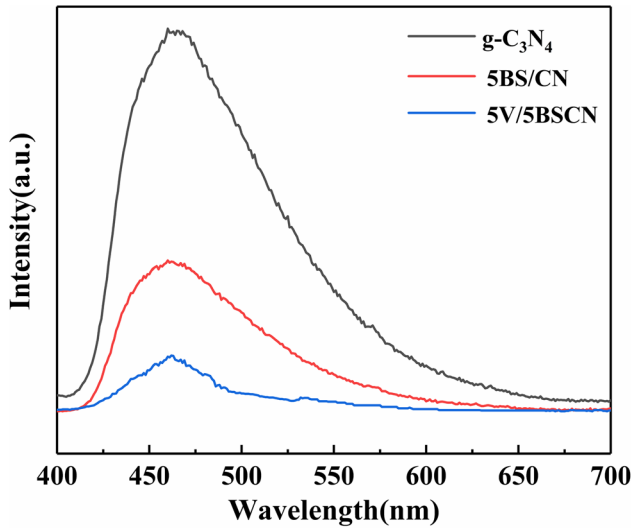


Fig. 12 PL spectra of g-C₃N₄, 5BS/CN and 5 V/5BSCN

Figure 14 shows the results of active species trapping experiments. It could be seen that the addition of TBA had almost no effect on the degradation rate of RB19, which indicated OH slightly participated in the photocatalytic degradation process. After adding BQ acting as a scavenger of O₂⁻, the degradation rate had a sharp decline. Also, AO slightly inhibited the reaction as h⁺ scavenger. Therefore, O₂⁻ played a main part during the photocatalytic reaction, and h⁺ was secondary. In order to further determine the main active species deciding RB19 degradation, NBT was introduced to the experiment. Figure 15 shows the spectra of the NBT transformation percentage in the presence of 5 V/5BSCN. As the photoreaction proceeded, NBT was gradually transformed, and the absorbance of NBT decreased significantly at

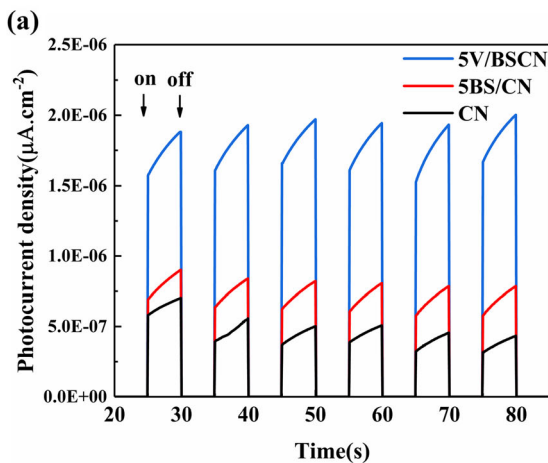


Fig. 13 Photocurrent response (a) and EIS measurements (b) of CN, 5BS/CN and 5 V/5BSCN

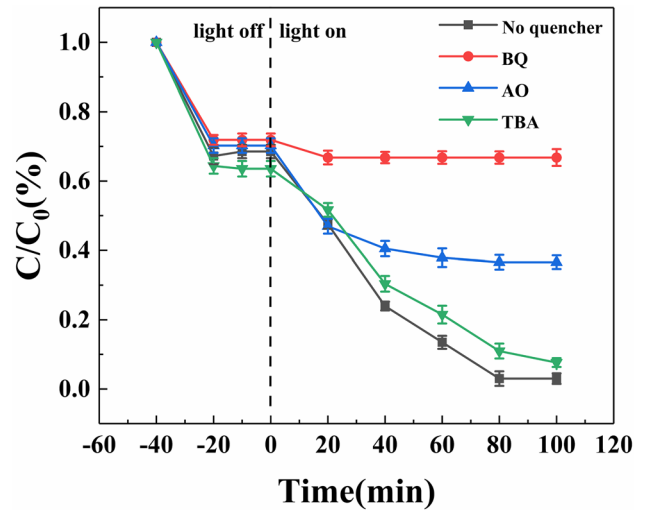
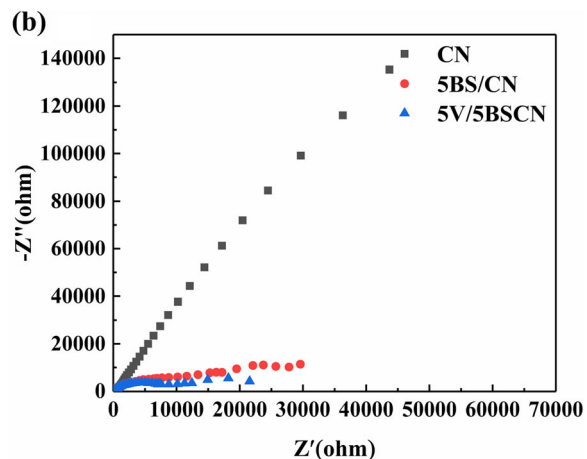


Fig. 14 Trapping experiment of 5 V/5BSCN photocatalysis (the dosage of catalyst = 0.8 g/L, C_{RB19} = 15 mg/L, pH 7.0)

120 min, which implied varieties of ·O₂⁻ radicals were generated during the process.

Based on the above analysis and band structure matching, dual Z-scheme path was favorable for the photocatalytic mechanism and charge transfer pathways of 5 V/5BSCN composite, as shown in Fig. 16. Under the irradiation of visible light, the electrons on the VB of Bi₂S₃, g-C₃N₄, and InVO₄ both were excited to CB, leaving holes on the VB, respectively. Then, the electrons on the CB of Bi₂S₃ and InVO₄ recombined with the holes on the VB of g-C₃N₄ through the heterojunction interface, and photogenerated electrons that accumulated on the CB of g-C₃N₄ reduced O₂ to O₂⁻, leading to the decomposition of RB19 molecules. Since the VB potential of Bi₂S₃ was



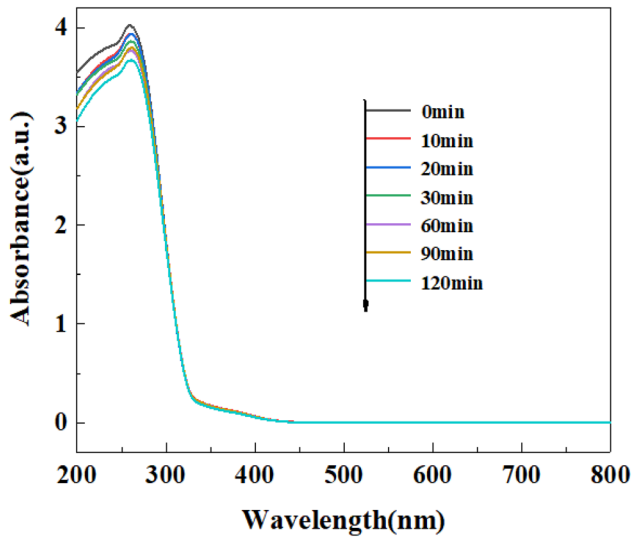
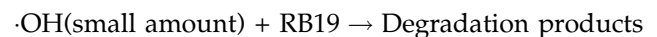
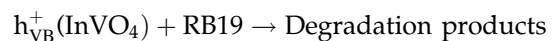
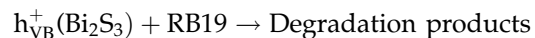
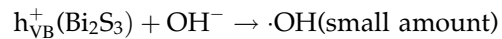
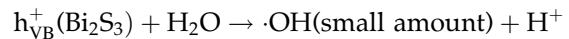
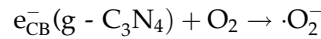
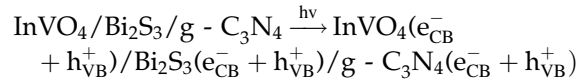


Fig. 15 UV–Vis absorbance spectra of Nitrotetrazolium Blue chloride aqueous solution containing 0.8 g/L of 5 V/5BSCN photocatalyst

positive than $E^0(\text{H}_2\text{O}/\text{OH})$ potential (1.99 eV *vs.* NHE), $\cdot\text{OH}$ radicals were generated on the VB of Bi_2S_3 . Meanwhile, the photogenerated holes left behind on the VB of InVO_4 would directly participate in the reaction of degrading RB19. In addition, because $g\text{-C}_3\text{N}_4$ accounted for the largest proportion of 5 V/5BSCN, O_2^- radicals generated by $g\text{-C}_3\text{N}_4$ were the main active species for oxidizing RB19 to degradation products, which was consistent with the results of the active species trapping and NBT conversion experiments. Therefore, the 5 V/5BSCN photocatalytic material realized the rapid separation of photogenerated carriers by constructing a dual Z-

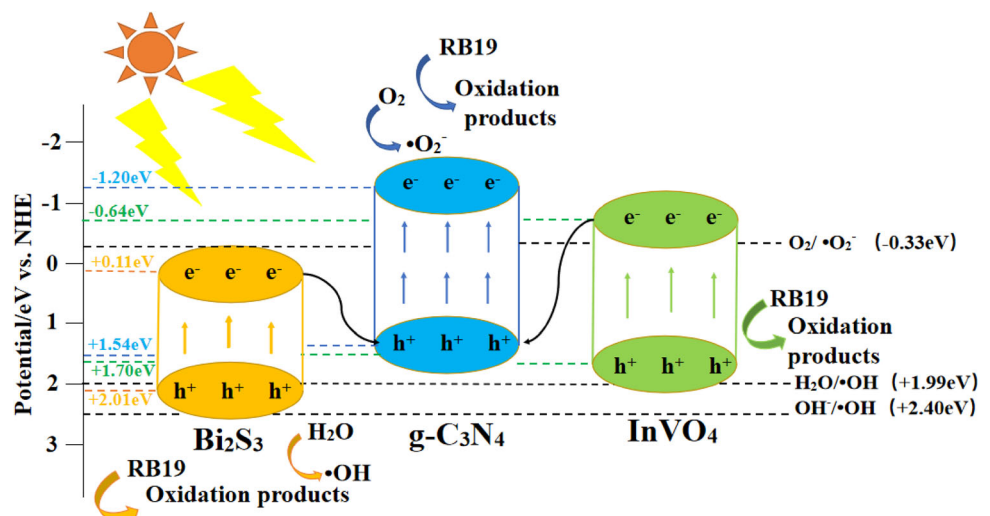
scheme heterojunction successfully, and improved the yield and lifetime of photogenerated carriers at the same time, which was also confirmed in the above-mentioned PL spectrum and electrochemical analysis results. The specific reaction process was shown in the following formula:



4 Conclusions

In summary, the ternary dual Z-scheme $\text{InVO}_4/\text{Bi}_2\text{S}_3/g\text{-C}_3\text{N}_4$ heterojunction photocatalyst was successfully synthesized by the wet impregnation method. Under visible light, the 5 V/5BSCN composite, i. e., the loading ratio of InVO_4 was 5%, performed the excellent photocatalytic degradation activity for RB19. After 100 min visible light irradiation, the degradation rate of RB19 achieved 95.5%. The improvement of the degradation rate of RB19 by $\text{InVO}_4/\text{Bi}_2\text{S}_3/g\text{-C}_3\text{N}_4$ was ascribed to generate tight

Fig. 16 Possible photocatalytic mechanism diagrams of 5 V/5BSCN



heterogeneous interfaces to construct the double Z-scheme heterostructure, which effectively inhibited the recombination of photogenerated carriers on the one hand, and enhanced the oxidation on the other hand. The active species trapping experiment showed that the role of free radicals in the degradation experiment followed $\cdot\text{O}_2^- > \text{h}^+ > \text{OH}$. According to the results of this experiment, the dual Z-scheme charges transfer mechanism could provide an effective strategy to design and fabricate g-C₃N₄-based nanocomposites for wastewater treatment.

Acknowledgements

This work was supported by the Natural Science Foundation of Shanxi (201901D111068) and Key Research and Development (R&D) Projects of Shanxi Province (201803D31152).

Author Contribution

YL: responsible for putting forward research ideas, designing research schemes, guiding, writing, editing, revising, and delivering paper. ST: responsible for doing some experiments, collecting and analyzing data, and writing paper. YM: responsible for the experiment and data analysis. YX: revising paper. LG: revising paper. WC: revising paper.

Funding

The funded was provided by Natural Science Foundation of Tianjin Municipal Science and Technology Commission (Grant No: 201901D111068), Key Research and Development (R&D) Projects of Shanxi Province (Grant No: 201803D31152).

Data availability

All data generated or analyzed during this study are included in this published article. And the original datasets generated during and/or analyzed during the current study are available from the corresponding author on reasonable request.

Declarations

Conflict of interest The authors declare that they have no known competing financial interests or personal relationships that could have appeared to influence the work reported in this paper.

Ethical approval The authors declare that the whole paper is original and related experiments have been carried out. The paper has not been submitted or published in other places, and it will not be submitted to other places until the program of periodical editorial department is completed. All the authors listed in the paper have agreed to sign their names and submit their papers for publication, and the order of authors has reached a consensus with all authors before submitting their papers.

References

1. S. Rajagopal, B. Paramasivam, K. Muniyasamy, Photocatalytic removal of cationic and anionic dyes in the textile wastewater by H₂O₂ assisted TiO₂ and micro-cellulose composites. *Sep. Purif. Technol.* **252**, 117444–117454 (2020)
2. C.T. Hou, H.Y. Liu, F.B. Mohammad, Preparation of ordered mesoporous F-H₂Ti₃O₇ nanosheets using orthorhombic HTiOF₃ as a precursor and their highly efficient degradation of tetracycline hydrochloride under simulated sunlight. *J Solid State Chem.* **300**, 122288–122302 (2021)
3. G. Gopal, S.A. Alex, N. Chandrasekaran, A. Mukherjee, A review on tetracycline removal from aqueous systems by advanced treatment techniques. *RSC Adv.* **10**, 27081–27095 (2020)
4. U. Rafiq, K. Majid, Mitigating the charge recombination by the targeted synthesis of Ag₂WO₄/Bi₂Fe₄O₉ composite: the facile union of orthorhombic semiconductors towards efficient photocatalysis. *J. Alloys Compd.* **842**, 155876–155884 (2020)
5. C.T. Hou, H.Y. Liu, Y.J. Li, The preparation of three-dimensional flower-like TiO₂/TiOF₂ photocatalyst and its efficient degradation of tetracycline hydrochloride. *RSC Adv.* **11**, 14957–14969 (2021)
6. H.J. Yu, Y.F. Zhao, C. Zhou, L. Shang, Y. Peng, Y.H. Cao, L.Z. Wu, C.H. Tung, T.R. Zhang, Carbon quantum dots/TiO₂ composites for efficient photocatalytic hydrogen evolution. *J. Mater. Chem. A.* **2**, 3344–3351 (2014)

7. W. Chen, Y.X. Hua, Y. Wang, T. Huang, T.Y. Liu, X.H. Liu, Two-dimensional mesoporous g-C₃N₄ nanosheet-supported MgIn₂S₄ nanoplates as visible-light-active heterostructures for enhanced photocatalytic activity. *J. Catal.* **349**, 8–18 (2017)
8. X. Zhang, X.Z. Yuan, L.B. Jiang, J. Zhang, H.B. Yu, H. Wang, G.M. Zeng, Powerful combination of 2D g-C₃N₄ and 2D nanomaterials for photocatalysis: recent advances. *Chem. Eng. J.* **390**, 124475–124503 (2020)
9. Y. Yang, C. Zhang, D.L. Huang, G.M. Zeng, J.H. Huang, C. Lai, C.Y. Zhou, W.J. Wang, H. Guo, W.J. Xue, R. Deng, M. Cheng, W.P. Xiong, Boron nitride quantum dots decorated ultrathin porous g-C₃N₄: Intensified exciton dissociation and charge transfer for promoting visible-light-driven molecular oxygen activation. *Appl. Catal. B.* **245**, 87–99 (2019)
10. Y. Yang, X. Li, C.Y. Zhou, W.P. Xiong, G.M. Zeng, D.L. Huang, C. Zhang, W.J. Wang, B.A. Song, X. Tang, X.P. Li, H. Guo, Recent advances in application of graphitic carbon nitride-based catalysts for degrading organic contaminants in water through advanced oxidation processes beyond photocatalysis: a critical review. *Water Res.* **184**, 116200–116217 (2020)
11. X.L. Liu, R. Ma, L. Zhuang, B.W. Hu, J.R. Chen, X.Y. Liu, X.K. Wang, Recent developments of doped g-C₃N₄ photocatalysts for the degradation of organic pollutants. *Crit. Rev. Environ. Sci. Technol.* **51**, 751–790 (2020)
12. L. Chen, Y.M. Xu, Z. Yang, K. Zhang, B.L. Chen, Cobalt (II)-based open-framework systems constructed on g-C₃N₄ for extraordinary enhancing photocatalytic hydrogen evolution. *Appl. Catal. B.* **277**, 119207–119215 (2020)
13. L. Zhou, H.Y. Zhang, H.Q. Sun, S.M. Liu, M.O. Tade, S.B. Wang, W.Q. Jin, Recent advances in non-metal modification of graphitic carbon nitride for photocatalysis: a historic review. *Catal. Sci. Technol.* **6**, 7002–7023 (2016)
14. X.J. Zhou, C.L. Shao, X.H. Li, X.X. Wang, X.H. Guo, Y.C. Liu, Three dimensional hierarchical heterostructures of g-C₃N₄ nanosheets/TiO₂ nanofibers: controllable growth via gas-solid reaction and enhanced photocatalytic activity under visible light. *J. Hazard. Mater.* **344**, 113–122 (2018)
15. F.F. Mei, K. Dai, J.F. Zhang, W.Y. Li, C.H. Liang, Construction of Ag SPR-promoted step-scheme porous g-C₃N₄/Ag₃VO₄ heterojunction for improving photocatalytic activity. *Appl. Surf. Sci.* **488**, 151–160 (2019)
16. S.P. Huang, Z.Q. Wei, X.J. Wu, J.W. Shi, Optical properties and theoretical study of Mn doped ZnAl₂O₄ nanoparticles with spinel structure. *J. Alloys Compd.* **825**, 154004–154012 (2020)
17. J.H. Ma, Z.Q. Wei, L. Li, L. Ma, C. Li, S.P. Huang, Synthesis and photoelectrochemical properties of visible-light response g-C₃N₄@CdS heterojunctions photocatalyst. *Desalin. Water. Treat.* **231**, 287–296 (2021)
18. S.P. Huang, Z.Q. Wei, M.J. Ding, C. Li, Q. Lu, Photo-electrochemical and photocatalytic properties of hierarchical flower-like BiOI/CoFe₂O₄ nanocomposites synthesized by co-precipitation method. *Opt Mater.* **111**, 110643–110652 (2021)
19. M. Jourshabani, B.K. Lee, Z. Shariatinia, From traditional strategies to Z-scheme configuration in graphitic carbon nitride photocatalysts: recent progress and future challenges. *Appl. Catal. B.* **276**, 119157–119184 (2020)
20. Y.A. Wang, Y.Q. Zeng, X.Y. Chen, Q.Y. Wang, S.P. Wan, D.Y. Wang, W. Cai, F.J. Song, S.L. Zhang, Q. Zhong, Tailoring shape and phase formation: Rational synthesis of single-phase BiFeWO_x nanooctahedra and phase separated Bi₂WO₆-Fe₂WO₆ microflower heterojunctions and visible light photocatalytic performances. *Chem. Eng. J.* **351**, 295–303 (2018)
21. N.Q. Thang, A. Sabbah, L.C. Chen, K.H. Chen, T. Minh, P.V. Viet, High-efficient photocatalytic degradation of commercial drugs for pharmaceutical wastewater treatment prospects: a case study of Ag/g-C₃N₄/ZnO nanocomposite materials. *Chemosphere* **282**, 130971–130982 (2021)
22. W.H. Zhao, Z.Q. Wei, X.D. Zhang, M.J. Ding, S.P. Huang, S.G. Yang, Magnetic recyclable MnFe₂O₄/CeO₂/SnS₂ ternary nano-photocatalyst for photo-Fenton degradation. *Appl. Catal. A-Gen.* **593**, 117443–117452 (2020)
23. Y.F. Jia, H.X. Ma, C.L. Liu, Au nanoparticles enhanced Z-scheme Au-CoFe₂O₄/MoS₂ visible light photocatalyst with magnetic retrievability. *Appl. Surf. Sci.* **463**, 854–862 (2019)
24. S.Q. Liu, Y.Y. Liu, G.P. Dai, X.Q. Bao, N. Huang, R. Peng, Y. Zhou, Synthesis and characterization of novel Bi₂S₃/BiOCl/g-C₃N₄ composite with efficient visible-light photocatalytic activity. *Mater. Lett.* **241**, 190–193 (2019)
25. W.H. Zhao, Z.Q. Wei, X.D. Zhang, M.J. Ding, S.P. Huang, PH-controlled MnFe₂O₄@ SnS₂ nanocomposites for the visible-light photo-Fenton degradation. *Mater. Res. Bull.* **124**, 110749–110755 (2020)
26. Y.J. Wang, J.R. Jin, W.G. Chu, D. Cahen, T. He, Synergistic effect of charge generation and separation in epitaxially grown BiOCl/Bi₂S₃ nano-heterostructure. *ACS Appl. Mater. Interfaces* **10**, 15304–15313 (2018)
27. Q. Hao, C. Xie, Y.M. Huang, D.M. Chen, Y.W. Liu, W. Wei, B.J. Ni, Accelerated separation of photogenerated charge carriers and enhanced photocatalytic performance of g-C₃N₄ by Bi₂S₃ nanoparticles. *Chin. J. Catal.* **41**, 249–258 (2020)
28. T.P. Hu, K. Dai, J.F. Zhang, G.P. Zhu, C.H. Liang, One-pot synthesis of step-scheme Bi₂S₃/porous g-C₃N₄ heterostructure for enhanced photocatalytic performance. *Mater. Lett.* **257**, 126740–126743 (2019)

29. J.D. Hu, D.Y. Chen, N.J. Li, Q.F. Xu, H. Li, J.H. He, J.M. Lu, Fabrication of graphitic-C₃N₄ quantum dots/graphene-InVO₄ aerogel hybrids with enhanced photocatalytic NO removal under visible-light irradiation. *Appl. Catal. B*. **236**, 45–52 (2018)
30. W.L. Shi, F. Guo, J.B. Chen, G.B. Che, X. Lin, Hydrothermal synthesis of InVO₄/graphitic carbon nitride heterojunctions and excellent visible-light-driven photocatalytic performance for rhodamine B. *J. Alloys Compd.* **612**, 143–148 (2014)
31. K. Saravanakumar, C.M. Park, Rational design of a novel LaFeO₃/g-C₃N₄/BiFeO₃ double Z-scheme structure: photocatalytic performance for antibiotic degradation and mechanistic insight. *Chem. Eng. J.* **423**, 130076–130087 (2021)
32. R. Rajendran, S. Vignesh, A. Sasireka, P. Priya, S. Suganthi, V. Raj, J.K. Sundar, M. Srinivasan, S. AlFaify, Investigation on novel Cu₂O modified g-C₃N₄/ZnO heterostructures for efficient photocatalytic dye degradation performance under visible-light exposure. *Colloids Interface Sci. Commun.* **44**, 100480–100490 (2021)
33. E. Jang, D.W. Kim, S.H. Hong, Y.M. Park, T.J. Park, Visible light-driven g-C₃N₄@ZnO heterojunction photocatalyst synthesized via atomic layer deposition with a specially designed rotary reactor. *Appl. Surf. Sci.* **487**, 206–210 (2019)
34. Z. Cui, H. Yang, X. Zhao, Enhanced photocatalytic performance of g-C₃N₄/Bi₄Ti₃O₁₂ heterojunction nanocomposites. *Mater. Sci. Eng. B*. **229**, 160–172 (2018)
35. M.T. Zhu, T.A. Kurniawan, F. Song, T. Ouyang, M.H.D. Othman, M. Rezakazemi, S. Shirazian, Applicability of BaTiO₃/graphene oxide (GO) composite for enhanced photodegradation of methylene blue (MB) in synthetic wastewater under UV-vis irradiation. *Environ. Pollut.* **255**, 113182–113191 (2019)
36. X.Q. Geng, S. Chen, X. Lv, W. Jiang, T.H. Wang, Synthesis of g-C₃N₄/Bi₅O₇I microspheres with enhanced photocatalytic activity under visible light. *Appl. Surf. Sci.* **462**, 18–28 (2018)
37. X.Y. Weng, B.Q. Shi, A.N. Liu, J.Y. Sun, Y. Xiong, H.Q. Wan, S.R. Zheng, L. Dong, Y.W. Chen, Highly dispersed Pd/modified-Al₂O₃ catalyst on complete oxidation of toluene: role of basic sites and mechanism insight. *Appl. Surf. Sci.* **497**, 143747–143757 (2019)
38. M. Pirhashemi, A. Habibi-Yangjeh, Simple and large scale one-pot method for preparation of AgBr-ZnO nanocomposites as highly efficient visible light photocatalyst. *Appl. Surf. Sci.* **283**, 1080–1088 (2013)
39. H.N. Che, G.B. Che, H.J. Dong, W. Hu, H. Hu, C.B. Liu, C.M. Li, Fabrication of Z-scheme Bi₃O₄Cl/g-C₃N₄ 2D/2D heterojunctions with enhanced interfacial charge separation and photocatalytic degradation various organic pollutants activity. *Appl. Surf. Sci.* **455**, 705–716 (2018)
40. W.L. Shi, M.Y. Li, X.L. Huang, H.J. Ren, C. Yan, F. Guo, Facile synthesis of 2D/2D Co₃(PO₄)₂/g-C₃N₄ heterojunction for highly photocatalytic overall water splitting under visible light. *Chem. Eng. J.* **382**, 122960–122968 (2020)
41. K.D. Zhong, J.W. Feng, H.B. Gao, Y.M. Zhang, K.R. Lai, Fabrication of BiVO₄@g-C₃N₄(100) heterojunction with enhanced photocatalytic visible-light-driven activity. *J. Solid State Chem.* **274**, 142–151 (2019)
42. S. Li, Z.R. Wang, X.Y. Xie, G.W. Liang, X.W. Cai, X.L. Zhang, Z.W. Wang, Fabrication of vessel-like biochar-based heterojunction photocatalyst Bi₂S₃/BiOBr/BC for diclofenac removal under visible LED light irradiation: mechanistic investigation and intermediates analysis. *J. Hazard. Mater.* **391**, 121407–121419 (2020)
43. N. Askari, M. Beheshti, D. Mowla, M. Farhadian, Synthesis of CuWO₄/Bi₂S₃ Z-scheme heterojunction with enhanced cephalexin photodegradation. *J. Photochem. Photobiol. A-Chem.* **394**, 112463–112476 (2020)
44. X. Zhang, J. Zhang, J.Q. Yu, Y. Zhang, F.K. Yu, L. Jia, Y.L. Tan, Y.M. Zhu, B.R. Hou, Enhancement in the photocatalytic antifouling efficiency over cherimoya-like InVO₄/BiVO₄ with a new vanadium source. *J. Colloid Interface Sci.* **533**, 358–368 (2019)
45. X.S. Zhao, Y.Y. You, S.B. Huang, Y.X. Wu, Y.Y. Ma, G. Zhang, Z.H. Zhang, Z-scheme photocatalytic production of hydrogen peroxide over Bi₄O₅Br₂/g-C₃N₄ heterostructure under visible light. *Appl. Catal. B-Environ.* **278**, 119251–119261 (2020)
46. Y.J. Wang, X.J. Bai, C.S. Pan, J. He, Y.F. Zhu, Enhancement of photocatalytic activity of Bi₂WO₆ hybridized with graphite-like C₃N₄. *J. Mater. Chem.* **22**, 11568–11573 (2012)
47. S.V.P. Vattikuti, P.C. Nagajyothi, J. Shim, Fabrication of CdS quantum dot/Bi₂S₃ nanocomposite photocatalysts for enhanced H₂ production under simulated solar light. *J. Mater. Sci. Mater. Electron.* **30**, 5681–5690 (2019)
48. X. Lin, X.Y. Guo, W.L. Shi, F. Guo, G.B. Che, H.J. Zhai, Y.S. Yan, Q.W. Wang, Ag₃PO₄ quantum dots loaded on the surface of leaf-like InVO₄/BiVO₄ heterojunction with enhanced photocatalytic activity. *Catal. Commun.* **71**, 21–27 (2015)
49. C. Yang, Q.Y. Tan, Q. Li, J. Zhou, J.J. Fan, B. Li, J. Sun, K.L. Lv, 2D/2D Ti₃C₂ MXene/g-C₃N₄ nanosheets heterojunction for high efficient CO₂ reduction photocatalyst: Dual effects of urea. *Appl. Catal. B* **268**, 118738–118748 (2020)
50. M. Chen, C.S. Guo, S. Hou, J.P. Lv, Y. Zhang, H. Zhang, J. Xu, A novel Z-scheme AgBr/P-g-C₃N₄ heterojunction photocatalyst: excellent photocatalytic performance and photocatalytic mechanism for ephedrine degradation. *Appl. Catal. B* **266**, 118614–118626 (2020)
51. C.Z. Zhu, T.T. Gong, Q.M. Xian, J.M. Xie, Graphite-like carbon nitride coupled with tiny Bi₂S₃ nanoparticles as 2D/

- OD heterojunction with enhanced photocatalytic activity. *Appl. Surf. Sci.* **444**, 75–86 (2018)
52. Y.F. Li, R.X. Jin, X. Fang, Y. Yang, M. Yang, X.C. Liu, Y. Xing, S.Y. Song, In situ loading of Ag_2WO_4 on ultrathin $\text{g-C}_3\text{N}_4$ nanosheets with highly enhanced photocatalytic performance. *J. Hazard. Mater.* **313**, 219–228 (2016)
53. N. Tian, H.W. Huang, Y. He, Y.X. Guo, T.R. Zhang, Y.H. Zhang, Mediator-free direct z-scheme photocatalytic system: $\text{BiVO}_4/\text{g-C}_3\text{N}_4$ organic-inorganic hybrid photocatalyst with highly efficient visible-light-induced photocatalytic activity. *Dalton Trans.* **44**, 4297–4307 (2015)
54. J.J. Xi, H. Wang, B.H. Zhang, F.Q. Zhao, B.Z. Zeng, Novel molecularly imprinted photoelectrochemical sensor for rutin based on $\text{Bi}_2\text{S}_3/\text{ZnIn}_2\text{S}_4$ heterojunction. *Sens. Actuators B-Chem.* **320**, 128409–128416 (2020)
55. U. Lamdab, K. Wetchakun, S. Phanichphant, W. Kangwan-supamonkon, N. Wetchakun, $\text{InVO}_4\text{-BiVO}_4$ composite films with enhanced visible light performance for photodegradation of methylene blue. *Catal. Today* **278**, 291–302 (2016)
56. Y. Chen, K.R. Liu, Preparation and characterization of nitrogen-doped TiO_2 /diatomite integrated photocatalytic pellet for the adsorption-degradation of tetracycline hydrochloride using visible light. *Chem. Eng. J.* **302**, 682–696 (2016)
57. Y.C. Deng, L. Tang, C.Y. Feng, G.M. Zeng, J.J. Wang, Y.Y. Zhou, Y.N. Liu, B. Peng, H.P. Feng, Construction of plasmonic Ag modified phosphorous-doped ultrathin $\text{g-C}_3\text{N}_4$ nanosheets/ BiVO_4 photocatalyst with enhanced visible-near-infrared response ability for ciprofloxacin degradation. *J. Hazard. Mater.* **344**, 758–769 (2018)
58. M. Yasmina, K. Mourad, S.H. Mohammed, C. Khaoula, Treatment heterogeneous photocatalysis; factors influencing the photocatalytic degradation by TiO_2 . *Energy Procedia* **50**, 559–566 (2014)
59. A. Nezamzadeh-Ejehieh, M. Karimi-Shamsabadi, Decolorization of a binary azo dyes mixture using CuO incorporated nanozeolite-X as a heterogeneous catalyst and solar irradiation. *Chem. Eng. J.* **228**, 631–641 (2013)
60. R.P.F. Melo, E.L.B. Neto, M.C.P.A. Moura, T.N.C. Dantas, A.A.D. Neto, H.N.M. Oliveira, Removal of Reactive Blue 19 using nonionic surfactant in cloud point extraction. *Sep. Purif. Technol.* **138**, 71–76 (2014)
61. C.Y. Jin, M. Wang, Z.L. Li, J. Kang, Y. Zhao, J. Han, Z.M. Wu, Two dimensional $\text{Co}_3\text{O}_4/\text{g-C}_3\text{N}_4$ Z-scheme heterojunction: mechanism insight into enhanced peroxymonosulfate-mediated visible light photocatalytic performance. *Chem. Eng. J.* **398**, 125569–125582 (2020)
62. M. Humayun, Z.W. Hu, A. Khan, W. Cheng, Y. Yuan, Z.P. Zheng, Q.Y. Fu, W. Luo, Highly efficient degradation of 2,4-dichlorophenol over $\text{CeO}_2/\text{g-C}_3\text{N}_4$ composites under visible-light irradiation: detailed reaction pathway and mechanism. *J. Hazard. Mater.* **364**, 635–644 (2019)
63. F. Raziq, Y. Qu, X.L. Zhang, M. Humayun, J. Wu, A. Zada, H.T. Yu, X.J. Sun, L.Q. Jingo, Enhanced cocatalyst-free visible-light activities for photocatalytic fuel production of $\text{g-C}_3\text{N}_4$ by trapping holes and transferring electrons. *J. Phys. Chem. C* **120**, 98–107 (2015)
64. C.J. Zhang, M.Y. Jia, Z.Y. Xu, W.P. Xiong, Z.H. Yang, J. Cao, H.H. Peng, H.Y. Xu, Y.P. Xiang, Y. Jing, Constructing 2D/2D $\text{N-ZnO/g-C}_3\text{N}_4$ S-scheme heterojunction: efficient photocatalytic performance for norfloxacin degradation. *Chem. Eng. J.* **430**, 132652–132661 (2022)
65. M.L. Tang, Y.H. Ao, C. Wang, P.F. Wang, Facile synthesis of dual Z-scheme $\text{g-C}_3\text{N}_4/\text{Ag}_3\text{PO}_4/\text{AgI}$ composite photocatalysts with enhanced performance for the degradation of a typical neonicotinoid pesticide. *Appl. Catal. B* **266**, 118614–118626 (2020)

Publisher's Note Springer Nature remains neutral with regard to jurisdictional claims in published maps and institutional affiliations.